

PACS: 42.79. Ci

Tunable high-finesse narrow bandpass Fabry – Perot filter

V.B. Markov¹, A.I. Khizhnyak¹, V. Goren^{1,2}, W.B. Cook³

¹ MetroLaser, Inc., 2572 White Rd., Irvine, CA 92614, USA

² University of California, Irvine, CA 92697, USA

³ NASA Langley Research Center, Hampton, VA 23681, USA

Abstract. This paper discusses the results of the analysis and experimental characterization of a narrow bandpass optical filter based on the Fabry – Perot interferometer configuration with a variable spacing between the mirrors allowing for a relatively wide spectral tunability. Such a filter, with a high-throughput bandpass and sufficiently large aperture and acceptance angle, is of practical interest for a high-resolution spectrometry and remote sensing in the visible and infrared spectral regions. The Fabry – Perot filter (FPF) can be designed in a compact single-assembly architecture that can be accommodated within existing instruments and should provide a stable performance under variable thermal and mechanical conditions, including space and airborne platforms. Possible applications of the filter include high-resolution multi-spectral imaging, terrain mapping, atmosphere and surface parameters measurements, and detection of chemical and biological agents.

Keywords: imaging Fabry – Perot interferometer, bandpass, optical throughput.

Manuscript received 30.11.04; accepted for publication 16.12.04.

1. Introduction

The Fabry – Perot interferometer (FPI) is a well established optical instrument with a long history of successful applications in different areas of spectroscopy, from remote sensing, fundamental length measurements of atomic and molecular lines, study of emission lines of the gaseous nebulas, to efficient optical elements for high-resolution laser wavelength tuning. As a matter of fact, an interferogram of the Orion Nebula using “nebulous line” by Buisson, Fabry and Bourget [1] served as the first illustration of the unique spectroscopic capabilities of the instrument. The use of FPI in astronomy in the early years was conducted mostly in France until it was realized [2] that due to the instrument’s high resolving and light gathering power it has tremendous advantage over the prism-based spectroscopic instruments. Although the first demonstration of scanning FPI was demonstrated more than a hundred year ago by Jobin in 1899 and described by Fabry in 1923, it was not until the laser era that the engineering development of the FPI really took off. Variety of the applications associated with laser measurements (high-resolution spectroscopy, lidars, laser wavelength tuning, etc.) required the instruments with a broadband operational capabilities, high throughput, high finesse and low losses. Progress in dielectric coating addressed some these problems, while the high resolution scanning nowadays is mostly achieved with piezoactuators or piezoelectric translators.

Improvement in the performance of the FPI based system was investigated by using holographic reflectors in both reflection [3] and transmission [4] modes as well as with multiplexed FPI configuration [5]. Specific configuration and requirements for the FPI are dictated by a particular area of application, and this paper studies the features of the high-resolution tunable FPI to be used for imaging spectroscopy.

High-resolution imaging spectroscopy and remote sensing applications require a tunable narrow bandpass filter with high throughput and low background noise [6-8]. As necessitated by the anticipated applications, the characteristics of such a filter should satisfy the following conditions [8]: the bandpass width $\Delta_p \lambda < 10^{-4}$ of the operational wavelength λ and tuning range $\Delta_f \lambda > 10^{-2} \lambda$, optical throughput up to 50 %, background rejection up to 40 dB, angular acceptance up to 1° , and an open aperture diameter up to 50 mm. Such requirements, in principle, can be met by using the filter in FPI configuration – the Fabry – Perot filter (FPF).

A typical optical FPF is formed by two flat mirrors with a spacer of variable optical length. The spacer (cavity) induces the narrow-width high-transmission resonant mini-bands (bandpasses) [9] within a wide reflection band of the mirrors, as shown schematically in Fig. 1. These bandpasses are associated with the localized modes formed by a cavity defect in a structure that resembles the photonic crystal formed by the multi-layer mirrors [10-12]. A very thin mirror spacer (of the order of $100 \times \lambda$) allows for a wide tuning range. High-precision

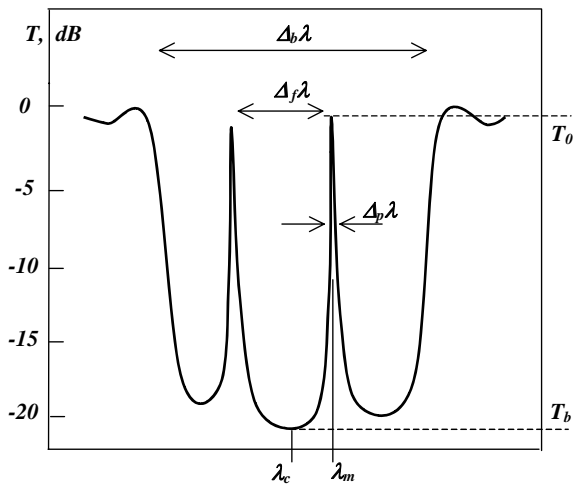


Fig. 1. Transmissivity function $T(\lambda)$ of a FPF with a narrow spacing, exhibiting a reflection band and two transmission mini-bands. The critical FPF parameters are: the reflection band central wavelength (λ_c) and width ($\Delta_b\lambda$); the bandpass peak wavelength (λ_m), width ($\Delta_p\lambda$) and tuning range ($\Delta_r\lambda$); background (T_b) and peak (T_0) transmissivity.

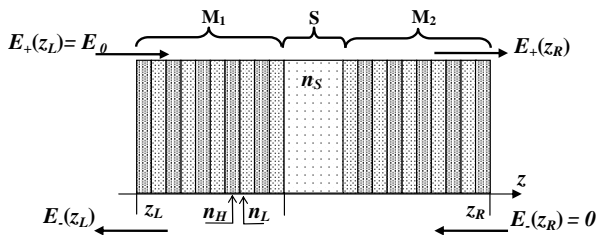


Fig. 2. Schematic diagram of the wave propagation through the Fabry-Perot filter with multi-layer dielectric mirrors.

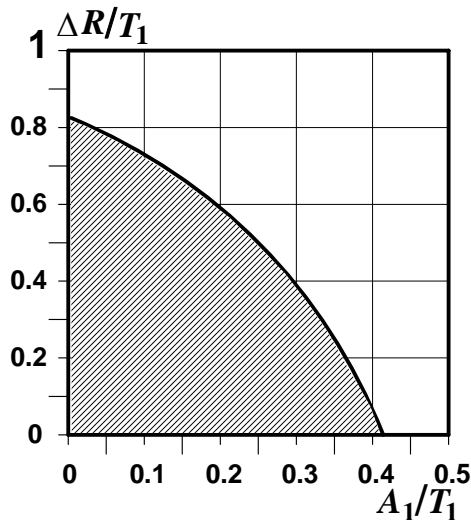


Fig. 3. The filter maximum transmissivity T_0 exceeds 50% level in the shaded area.

control of the spacer thickness allows for tuning the bandpass wavelength as well as for active compensation of instabilities associated with thermal and mechanical effects.

The essential characteristics of the FPF [9] are: its maximum (T_0) and background (T_b) transmissivity that determine the bandpass throughput and background rejection; the finesse that is the ratio between the bandpass free tuning range and its width; the interference phase shift at the spacer-mirror interface that yields a correction to the bandpass position [13-16], the latter being important for a narrow-bandpass and/or widely-tunable filter. In this paper, we perform an analysis and experimental studies of all these parameters for the FPF.

2. Description of the FPF

In our model the FPF is formed by two flat dielectric mirrors (M_1 and M_2) made of alternating layers of material with higher (n_H) and lower (n_L) refractive index. The mirrors are separated by a homogeneous dielectric spacer (S) with refractive index n_S (see schematic in Fig. 2). The transmissivity and reflectivity for such a multilayer optical element are defined based on the superposition of the plane monochromatic waves $E_{\pm}(z)$ propagating forward (+) and backward (-) along the z -axis,

$$E(z) = E_+(z) + E_-(z),$$

$$E_{\pm}(z) = A_{\pm} \exp(\mp i k_n z), \quad (1)$$

$$k_n = nk, \quad k = 2\pi/\lambda$$

where the amplitudes A_{\pm} are constant within each homogeneous layer, but their values change from one layer to another (k and λ are the wavevector and the wavelength in a vacuum, and k_n is the wavenumber inside the medium with refractive index n).

Given a wave incident onto the system from the left (forward), and no backward incident wave (see Fig. 2),

$$E_+(z_L) = E_0 \neq 0, \quad E_-(z_R) = 0, \quad (2)$$

the filter transmission and reflection coefficients are

$$t = E_+(z_R)/E_0, \quad r = E_-(z_L)/E_0 \quad (3)$$

and the transmissivity and reflectivity of the filter are

$$T = |t|^2, \quad R = |r|^2, \quad (4)$$

assuming that the filter has the same dielectric medium adjacent to it on both sides.

3. Characterization of the FPF transmission

3.1. FPF transmissivity in terms of the mirror characteristics

The solution of the wave equation in the homogeneous medium of the spacer permits to express the FPF transmissivity in as [9]:

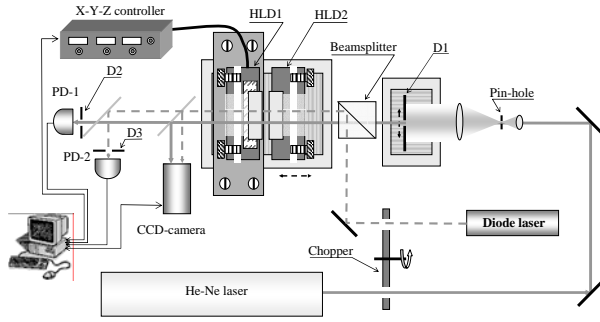


Fig. 4. Schematic of the experimental set-up.

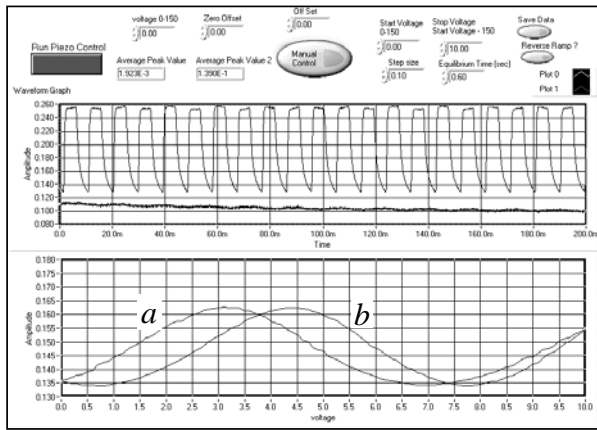


Fig. 5. PC screen showing the photodiode PD output signal (upper trace) and the Michelson interferometer transmittance (lower trace) vs. incremental (a) and decremented (b) voltage applied to the piezo actuator.

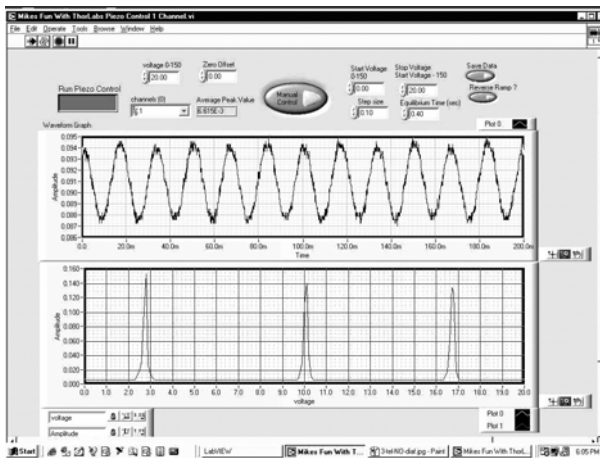


Fig. 6. Experimental dependence of the light intensity on the filter output with incremental voltage applied to piezo actuator.

$$T = T_0 \left[1 + F \sin^2(\varphi_T) \right]^{-1}, \quad (5)$$

where maximum transmissivity T_0 and the F -factor can be expressed in terms of the transmissivity (T_1, T_2) and reflectivity (R_1, R_2) of the mirrors M_1 and M_2 , as follows:

$$T_0 = T_1 T_2 / \left(1 - \sqrt{R_1 R_2} \right)^2, \quad (6)$$

$$F = 4\sqrt{R_1 R_2} / \left(1 - \sqrt{R_1 R_2} \right)^2, \quad (7)$$

and φ_T is the total interference phase:

$$\varphi_T = kn_S L_S - \varphi_M. \quad (8)$$

Here $kn_S L_S$ is the optical length of the spacer (L_S is the mirror spacing thickness), and the phase shift φ_M is the median phase of the reflection coefficients of the two mirrors, determined by the structure of the multi-layer mirrors (Fig. 2):

$$\varphi_M = (\varphi_{r1} + \varphi_{r1}) / 2, \quad \varphi_{rj} = \arg(r_j), \quad |\varphi_M| \leq \pi, \quad (9)$$

Eqs (6) - (9) can be derived in a consistent way [17] using the transfer matrix approach [18]. The phase shift φ_r upon reflection from a dielectric multi-layer mirror has nearly linear dependence on the wavevector k near the center k_c of the reflection band [15-17],

$$\varphi_r(k) \cong -b\pi(k - k_c) / k_c, \quad \text{for } k - k_c \ll k_c \quad (10)$$

with the coefficient $b \sim 5 > 0$ at the realistic values of the parameters of the mirror. Therefore, the total interference phase shift φ_T in Eq. (8) is also a linear function of the wavevector,

$$\varphi_T(k) = k\Lambda_S - b\pi; \quad b = (b_1 + b_2) / 2, \quad (11)$$

where

$$\Lambda_S = n_S L_S + b\lambda_c / 2$$

is an effective optical length of the cavity spacer for central wavelength λ_c (Fig. 1). The value of Λ_S includes the contribution of $b\lambda_c / 2$ that can be interpreted here as a mirror penetration length [15].

Based on the grating-mirror model with the coupled-wave approach [19], we have shown earlier [17] that linear dependence of the phase change φ_r on the wavevector (Eq. (10)) holds within the mid-band range up to a half-width $\Delta_b k$ of the reflection band of the multi-layer dielectric mirror,

$$|k - k_c| \leq 0.5\Delta_b k \cong 0.2(\Delta n / \bar{n})k_c \quad (12)$$

where $\Delta n = n_H - n_L$, and $\bar{n} = (n_H + n_L) / 2$ are the difference and median of the refractive indices of the mirror layers (see Fig. 2), while the band-center wavevector is $k_c = \pi / (\bar{n} \ell_M)$ and ℓ_M is the layer-pair thickness. The phase-shift coefficient b is

$$b \cong (n_S / \bar{n})^{\pm 1} (\bar{n} / \Delta n) \tanh(N\Delta n / \bar{n}) \quad (13)$$

for $n_S \leq \bar{n}$, where the sign (\pm) in the power depends on the value of the front layer refractive index, and is (+) for n_H and (-)

for n_L , respectively. N is the number of the layer pairs, and we assume that the refractive index of the substrate is matched to the median refractive index \bar{n} in the multi-layer coating. (If $n_S > \bar{n}$, then n_S and \bar{n} have to be switched in the first two factors in Eq. (13)).

3.2. Bandpass spectral position, free range, and tuning range

It follows from Eq. (5) and (11) that the spectral positions k_m of the bandpass maxima are:

$$k_m = (m + b)\pi / \Lambda_S, \quad m = 1, 2, \dots \quad (14)$$

Therefore, regardless the bandpass number m , the bandpass free range in terms of the wavevector is

$$\Delta_f k = \pi / \Lambda_S. \quad (15)$$

Because the free range defined by Eq.(15) has to be larger than the required tuning range, $\Delta_f k \geq \Delta_t k$, the spacer length should be small enough and should satisfy the following condition

$$\Lambda_S \leq \delta_t^{-1} \lambda_c / 2, \quad (16)$$

where $\delta_t = \Delta_t k / k_c$ is the relative value of the required tuning range ($\delta_t \cong \Delta_t \lambda_m / \lambda_c$ for $\lambda_m \approx \lambda_c$). If a relatively wide tuning range is of interest ($\delta_t \geq 0.02$), then the phase-shift contribution (with $b \sim 5$) to the spacer effective length Λ_S is significant for determining the relation of the free range (Eq. (15)) to the mirror spacing L_S . The value of L_S required to position the bandpass peak at the center of the reflection band can be found from Eq. (14):

$$n_S L_S = m_c \lambda_c / 2 \quad (17)$$

where m_c is the number of this bandpass. According to the definition of Λ_S , the corresponding relative value of the free range (Eq. (15)) is related to this bandpass number as

$$\delta_f = \Delta_f k / k_c = 1 / (m_c + b). \quad (18)$$

To meet the requirement of Eq. (16) this bandpass number should satisfy the condition $m_c \leq \delta_t^{-1} - b$, so the mirror spacing should be small according to Eq. (17). For a typical requirement of $\delta_t \sim 0.01$, this yields the following restrictions: $m_c \leq 90$ and $n_S L_S \leq 45 \lambda_S$.

3.3. Bandpass spectral width

According to Eq. (5) for the FPF transmissivity, the bandpass width (at half-maximum) in terms of the interference phase shift φ_T is equal to $2/\sqrt{F}$ at $F \gg 1$, while the phase spacing between the adjacent bandpass peaks is equal to π . Thus, the phase shift ratio of the bandpass spacing over the width (the interferometer finesse [9]) is

$$f = (\pi/2)\sqrt{F}. \quad (19)$$

The same ratio (regardless of the bandpass number m) holds between the bandpass spectral width ($\Delta_p k$) and free range (Eq. (15)) in terms of the wavevector,

$$\Delta_p k = \Delta_f k / f, \quad (20)$$

and between their relative values,

$$\delta_p = \Delta_p k / k_c = \delta_f / f = 1 / (m_c + b) f, \quad (21)$$

where m_c is the number of bandpass as defined by Eq. (17).

It follows from this analysis that if $\delta_t = 0.01$ and $\delta_p = 0.5 \cdot 10^{-4}$ are of interest, then the finesse should be at least $f = 200$.

3.4. Control of the bandpass spectral position

For applications in a high-resolution spectroscopic imaging, the FPF bandpass peak position (k_m or $\lambda_m = 2\pi / k_m$) has to be controlled with high precision. In this analysis we assume that the precision control should be better than one-fifth of the bandpass width ($\Delta_p k$ or $\Delta_p \lambda$, see Fig. 1). Such a requirement restricts the tolerated relative error to (see Eq. (21)):

$$\tilde{\Delta} \lambda_m / \lambda_c \cong \tilde{\Delta} k_m / k_c \leq \delta_p / 5, \quad (22)$$

that is $\sim 10^{-5}$ for the narrow bandpass filter.

The spectral position of the bandpass peak is determined by the spacer optical length $n_S L_S$ that can be tuned by varying either the mirror spacing L_S or the spacer refractive index n_S . It follows from Eq. (14) that the peak wavelength is a linear function of the spacer optical length,

$$\lambda_m = (2n_S L_S + b\lambda_c) / (m + b). \quad (23)$$

Therefore, both the mirror spacing L_S and the refractive index n_S of the spacer have to be controlled with the same relative precision (Eq. (22))

$$\tilde{\Delta} L_S / L_S + \tilde{\Delta} n_S / n_S \leq \delta_p / 5. \quad (24)$$

Therefore (see Eqs (17) and (21)), the following absolute precision is required for the mirror spacing L_S :

that is $\tilde{\Delta} L_S \leq 0.3 \text{ nm}$ for $\lambda_c \cong 600 \text{ nm}$ with $f = 200$. Such a high precision can be achieved using piezoelectric actuators with closed-loop control [16].

Due to varying the spacer optical length the tuning coefficient for the bandpass peak wavelength Eq. (23) is

$$C_t = \Delta \lambda_m / \Delta (n_S L_S) = 2 / (m + b). \quad (26)$$

To shift the bandpass over its entire free range from the band center to an adjacent bandpass, the spacer optical length, according to Eq. (17), should be changed by $\Delta_f (n_S L_S) \cong \lambda_c / 2$. One can see that the influence of the phase-shift on the bandpass spectral position is significant for the precise tuning of a narrow bandpass within a wide free spectral range. According to Eqs (21)

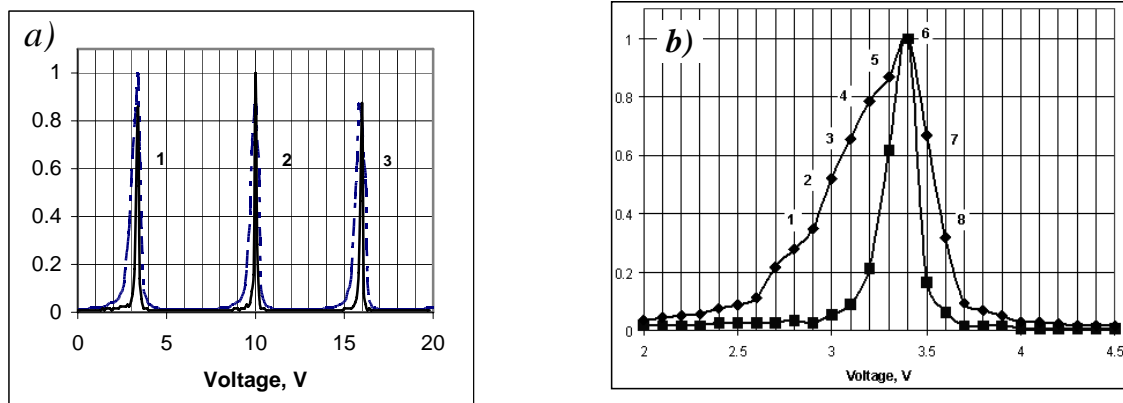


Fig. 7. Normalized intensity of transmitted light vs. voltage applied to piezo actuator. Solid line shows FPF transmission for diaphragm D1 of 4 mm diameter, and broken line is for transmission through total aperture. Figure (b) shows the details of the first peak in (a).

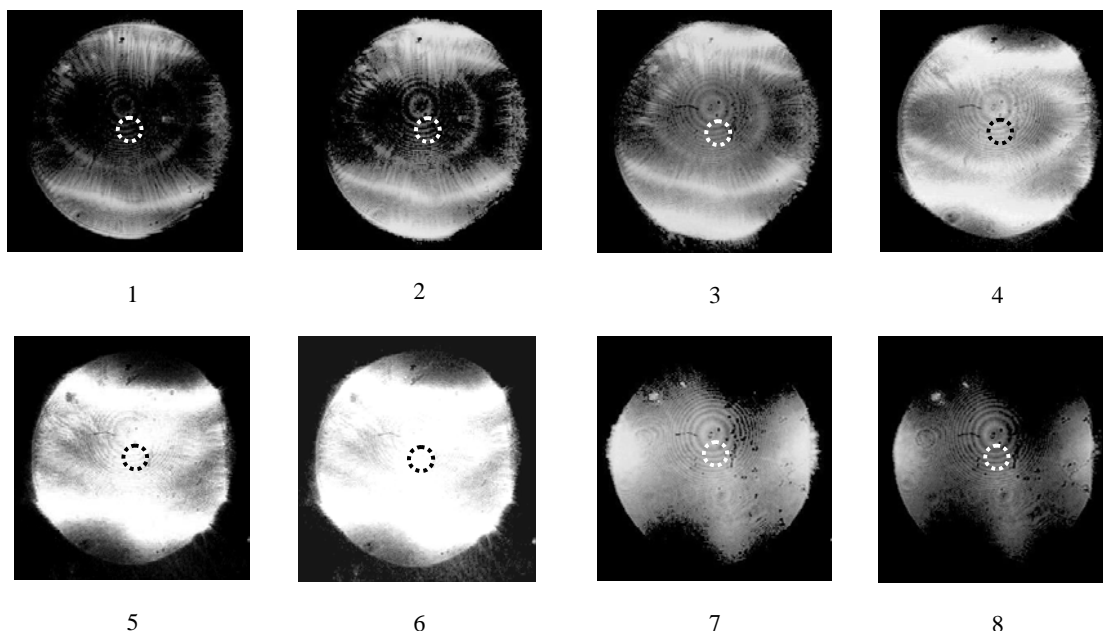


Fig. 8. Light distribution at the filter output when illuminated by the expanded laser beam (the diaphragm D1 in Fig. 4 is open). The circled area is for the output beam selected through the diaphragm D2 (Fig. 4). The numbers on the frames correspond to the numbers in Fig. 7 (b).

and (22), the phase-shift contribution (*b*-terms) in Eqs (23) and (26) has to be accounted when

$$(m_c + b)/f \equiv \delta_p / \delta_f^2 \leq 5b.$$

This is certainly the case for $\delta_f \geq 0.01$ and $\delta_p \leq 10^{-4}$ with $b \geq 1$.

4. Tolerance analysis

4.1. Requirements for FPF mirrors

It follows from Section 3 that in order to attain a high finesse ($f \geq 200$) needed to build a narrow-bandpass tunable FPF, it is essential that the reflectivity of the

mirrors should be close enough to 100 %. According to Eqs (7) and (19),

$$f = \pi\sqrt{\bar{R}} / (1 - \bar{R}), \quad (27)$$

where $\bar{R} = \sqrt{R_1 R_2}$ is an average reflectivity of the mirror pair. Therefore, for achieving the required filter finesse $f \gg 1$, the reflectivity \bar{R} has to satisfy the following condition

$$\bar{R} \cong 1 - \pi / f, \quad (28)$$

resulting in $\bar{R} \cong 0.984$ for $f = 200$. Note, that the relative error for the finesse (Eq. (27)) and, therefore, for the bandpass width (Eq. (21)) is the same for $(1 - \bar{R})$.

Following from Eq. (6) for the maximum transmissivity T_0 , an average transmissivity $\bar{T} = \sqrt{T_1 T_2}$ of the mirror pair is determined by T_0 and \bar{R} (or f) as:

$$\bar{T} = (1 - \bar{R})\sqrt{T_0} \cong \pi\sqrt{T_0} / f. \quad (29)$$

Thus, it follows from Eq. (29) that in order to achieve the maximum transmissivity $T_0 = 50\%$ with the finesse $f = 200$, an average transmissivity \bar{T} should be $\bar{T} \cong 0.011$.

Maximum transmissivity T_0 of the filter with a pair of identical lossless mirrors would be as high as 100 %. However, due to non-zero absorbance ($A > 0$) of the mirror structure, as follows from the energy balance, the magnitude of T_0 (in Eq. (6)) always remains lower than 100 %,

$$T_i = (1 - R_i) - A_i, \quad (i = 1, 2). \quad (30)$$

In order to satisfy the requirement of $T_0 \geq 50\%$, the absorbance of the mirror has to be low,

$$A_i / T_i \leq 0.4 \text{ or } A_i / (1 - R_i) \leq 0.3. \quad (31)$$

In addition, the maximum transmissivity T_0 (Eq. (6)) of the filter is reduced if the transmission characteristics of the two mirrors differ. Indeed, even without absorption, $\bar{T} < 1 - \bar{R}$ if $R_2 \neq R_1$. According to Eq.

(30) maximum transmissivity T_0 of the FPF can be approximated by the following function of the relative absorbance A_i / T_i and reflectivity difference $\Delta R / T$:

$$T_0 \cong (1 - \Delta R / T_i) / (1 + A_i / T_i - 0.5 \Delta R / T_i)^2, \quad (32)$$

where we denoted $\Delta R = R_2 - R_1 > 0$ and made a practically reasonable assumption $|A_2 - A_1| \ll \Delta R \ll R_1$. The graph of Eq. (32) with $T_0 = 0.5$ in the plane of variables A_i / T_i and $\Delta R / T_i$ confines the area where the maximum transmissivity is higher than 50 % (see Fig. 3).

According to Eqs (5) and (19), the background transmissivity T_b can be expressed as:

$$T_b = T_0 [1 + (2f / \pi)^2]^{-1}, \quad (33)$$

so that the filter background rejection level is determined entirely by its finesse f , and for $f \geq 200$, the background rejection is $T_0 / T_b \geq 1.6 \cdot 10^{-4} \geq 40$ dB.

4.2. Tolerance to the environmental variations

In order to control the peak wavelength position of the narrow bandpass ($\delta_p \cong 0.5 \cdot 10^{-4}$) with the precision defined by the requirements from Eq. (22), according to Eq. (24) the uncontrolled variations of the spacer refractive index n_s have to be limited as

$$\tilde{\Delta} n_s / n_s \leq \delta_p / 5 \cong 10^{-5}. \quad (34)$$

In its most common design, the FPF has an air spacer with $n_s = n_a$, where n_a is the refractive index of air. The value of n_a is close to 1.0 and varies upon the temperature t , atmospheric pressure P , and relative humidity H [20]. It is convenient to analyze the variations of n_a in terms of the air refractivity η_a ,

$$\eta_a = n_a - 1. \quad (35)$$

The requirement of Eq. (34) yields the limitation on the absolute variations of the air refractivity (Eq. (35)),

$$\tilde{\Delta} \eta_a \leq \delta_p / 5 \cong 10^{-5}. \quad (36)$$

At normal conditions, $t_0 = 15$ °C, $P_0 = 1000$ mb and $H_0 = 50\%$, the air refractivity is $\eta_{a0} \cong 27.2 \cdot 10^{-5}$ at $\lambda = 680$ nm. For small deviations of the environmental variables t , P , and H from normal conditions the dependence of the deviation of η_a from η_{a0} on these variables is practically linear [20]:

$$\eta_a - \eta_{a0} \cong 0.097(t - t_0) \cdot 10^{-5}, \quad (37)$$

$$\eta_a - \eta_{a0} \cong 0.027(P - P_0) \cdot 10^{-5}, \quad (38)$$

$$\eta_a - \eta_{a0} \cong 0.075 \cdot 10^{-2}(H - H_0) \cdot 10^{-5}. \quad (39)$$

Following from Eqs (37) - (39), the variations of the air parameters (near normal conditions) allows to tolerate the requirement of Eq. (36) within the following limits:

$$\tilde{\Delta} t \leq 10$$
 °C, $\tilde{\Delta} P \leq 37$ mb, $\tilde{\Delta} H \leq 100\%$. (40)

4.3. Angular acceptance of the FPF

For off-axis incidence (at an angle $\theta \neq 0$), Eq. (8) for the interference phase can be modified by replacing the absolute value of the wavevector by its z -component [9]. Therefore, the bandpass peak spectral position $k_{m\theta}$ is related to its value at normal incidence as:

$$k_{m\theta} \cos \theta = k_m. \quad (41)$$

The acceptance angle θ_a for a spectroscopic imaging FPF can be defined as an angle of incidence at which the bandpass peak shifts from its normal-incidence position by one-fifth of the bandpass width (in accordance with

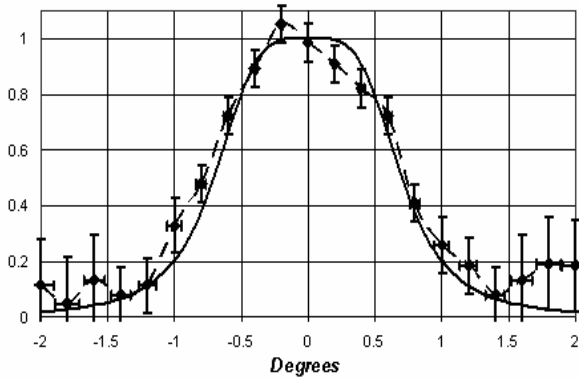


Fig. 9. Angular dependence of the normalized filter transmission as measured experimentally and calculated.

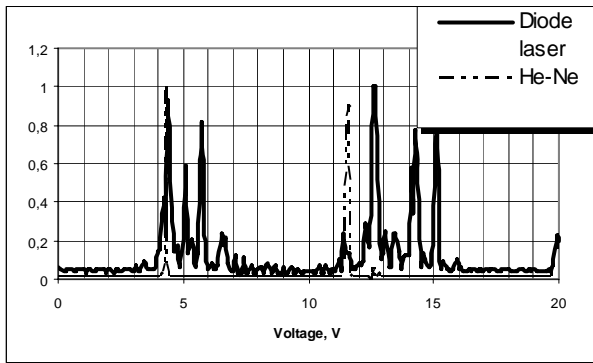


Fig.10. Normalized intensity of the transmitted light for two sources: diode laser $\lambda = 685$ nm, and He-Ne laser with $\lambda = 633$ nm.

the maximum tolerated error restriction of Eq. (21) and (22). Therefore,

$$\theta_a \cong \sqrt{0.4\delta_p} . \quad (42)$$

For the required spectral width of the bandpass $\delta_p \cong 0.5 \cdot 10^{-4}$, the acceptance angle is $\theta_a \cong 0.27^\circ$ and the total angular acceptance of the filter is $2\theta_a \cong 0.55^\circ$. Thus, the FPF can be used in spectral imaging systems as it transmits spectrally pure radiation within a sufficiently large solid angle at near-normal incidence and preserves the whole image of a remote object.

5. Experimental investigation of the filter

5.1. Experimental set-up

In performed experimental studies the FPF was formed by two high-reflectivity dielectric mirrors of 2.5 cm diameter placed in the holders for their mutual adjustment (Fig. 4). The ThorLabs KC1-PZ optical mount with 3-axes piezoactuators was used as one holder allowing for the mirror adjustment with

0.6 arc-sec precision. The mount was operated with the computer driven piezocontroller MDT693 from ThorLabs, Inc. The spacing between two mirrors was adjustable through the precision shift control platform with attached holder for the second mirror. All components of the breadboard were set on the vibration-isolated table that suppresses the relative random displacement of the mirrors constituting the FPF. A He-Ne laser was used as the source of the narrowband emission and its beam intensity was modulated with a chopper. The output laser beam was expanded to 5 cm diameter and it was cleaned up. 2.5 cm diameter central section of the beam with a homogeneous intensity distribution was used for the experiments and an iris diaphragm D1 was placed in front of FPF to cut off a narrow portion of the beam. Thus, for each position of the diaphragm the intensity at the FPF input remained the same.

The beam transmitted by the FPF (the output beam) was fed into photodiode (PD1) through an iris diaphragm for measuring the intensity in a narrow section of the beam. The second photodiode (PD2) without a diaphragm was used to register the total intensity of the beam. A CCD-camera connected to a computer performed registration of the transmission intensity of the FPF.

5.2. Characterization of the piezoactuator

The setup performance was characterized in an initial stage of experiments. In particular, we were interested in establishing the realistic specification of the KC1-PZ optical mount operation. For this to be done, this mount was placed in the Michelson interferometer. A typical variation in the intensity of the transmitted light is shown in Fig. 5, it illustrates the modulation in the transmittance of the Michelson interferometer as a function of the voltage applied to the piezoactuator with variable period of oscillation observed for increasing and decreasing voltages. The measured data reveal a hysteresis in the piezoactuator response.

It follows from these measurements that the piezoactuator we used has an average specific displacement (calibration coefficient) $\delta_z \cong 45$ nm/V.

5.3. Measurement of the filter transmission characteristics

Fig. 6 shows the computer screen in case of a small diaphragm D1 when the input beam is narrower than the total filter aperture. Fig. 7 illustrates the transmission of the FPF with the input beam diameter equal to 4 mm and the total aperture is open. It is evident from this figure that an increase of the FPF aperture results in transmission function broadening.

The observed difference can be attributed to flatness variations of the FPF mirrors. This conclusion is supported by the CCD-images shown in Fig. 8 that records the cross-sectional intensity distribution of the

transmitted beam. It shows a non-uniform intensity distribution with different maximum position for different values of the voltage applied to the piezoactuator. It follows from this data that the distance between the mirrors of the filter is a function due to the position along the mirror surface, which would be expected when the mirrors are non-planar.

In finding the shift of the mirror position for changing from the maximum transmission in the filter center to the maximum transmission at the boundary of the filter, we conclude that the mirrors are concave and estimate the difference of the mirror spacing between peripheries and the center as ≈ 9 nm, so the non-flatness of the mirrors across the one-inch diameter section is approximately $\lambda/70$ for $\lambda = 632.8$ nm.

5.4 Acceptance angle of the filter

The acceptance angle of the FPF was defined and measured as the FPF transmissivity at different incident angles of the incoming collimated laser beam. The intensity of the transmitted beam at its central part was measured for several values of the incident angle. The size of the diaphragm in front of the photodetector was selected to ensure minimal bandwidth at normal incidence. Fig. 9 illustrates a typical dependence of the detected signal upon angular deviation of the FPF, with every experimental point on the graph corresponding to an average value of multiple measurements, and with the solid line calculated from the expression

$$T = \frac{1}{1 + (2f/\pi)^2 \sin^2(\pi m_c \cos \theta)} \quad (43)$$

that describes the transmissivity of the FPF as the function of the incident angle for the bandpass at the center λ_c of the mirror reflection band (m_c is this bandpass number, see Eq. (17)).

The following values were used for calculating the transmissivity as the function of the incident angle: $\phi = 70$, $m_c = 2L_S/\lambda_c = 500$. The value of ϕ was estimated based upon the free range and spectral width of the bandpass at normal incidence of the laser beam, and the value of the parameter m_c follows from the spacer thickness equal to $L_S \approx 160$ μm . With these values, the free spectral range is $\Delta_f \lambda \approx 1.18$ nm, and the bandpass width is $\Delta_p \lambda \approx 0.017$ nm.

Fig. 9 shows a good correlation between the measured angular dependence of the transmissivity and Eq. (43), illustrating a low sensitivity of the acceptance angle to the mirror non-flatness. Indeed, for a given spacer thickness L_S and finesse ϕ , the total path ℓ of the beam inside the FPF can be estimated as $\ell = \phi \cdot 2L_S$, as the magnitude of finesse indicates the number of the interfering beams, i.e., the number of the passes through the interferometer. For the chosen values of the key parameters of the FPF this results in $\ell = 22.4$ mm. By tilting the FPF on 1° the spatial

displacement Δ_\perp of the beam across the window of the FPF is $\Delta_\perp = 0.38$ mm. Thus, the value of Δ_\perp is one-tenth of the selected beam diameter at the detector. These measurements suggest that for the conditions of the experiments, the non-flatness of the mirrors doesn't have a significant effect on the results obtained.

5.5 Broadband light source (diode laser) characterization

In this set of the experiments, a broadband light source was used for FPF characterization. The diode laser operating in a multi-frequency regime at $\lambda = 685$ nm served for this purpose. Fig. 10 shows that the FPF resolution is higher than the bandwidth of the diode-laser light. It is also evident from this figure that the distance between the corresponding peaks in the transmission function is different due to the wavelength difference between the He-Ne and diode lasers. If the displacement of the mirror is a linear function of the voltage applied to the piezoactuator, the simple relation between two transmission wavelengths holds:

$$\frac{V(\lambda_1)}{V(\lambda_2)} = \frac{\lambda_1}{\lambda_2}, \quad (44)$$

where $V(\lambda_n)$ is the voltage variation for tuning between two transmission maxima at the wavelengths λ_n . Our estimations satisfy Eq. (44) with an error rate of less than 5%.

Fig. 10 illustrates the difference in the structure of the spectrum for two orders of the FPF transmission. This is mostly due to the instability of the oscillating spectrum of the diode laser, what is typical when such a laser operates without stabilization of its characteristics.

6. Conclusions

In this paper, we present the results of the analysis and experimental characterization of a narrow bandpass tunable Fabry – Perot filter. It follows from the performed analysis that the contribution of the phase shift of the light wave at its reflection from the FPF mirrors to the effective optical length of the spacer plays an essential role in the precise spectral tuning of the filter bandpass. For the FPF with dielectric mirrors, we have shown analytically that the dependence of this phase shift on the wavevector is linear up to a half-width of the mirror reflection band, and derived a simple expression for the phase-shift coefficient in terms of the mirror parameters. It follows from the performed analysis that the phase shift has to be accounted for the filter with a bandpass width narrower than $\sim 10^{-4}$ and a tuning range wider than $\sim 10^{-2}$ of the operational wavelength.

We have also analyzed the tolerances to the absorbance of the mirror structure and reflectivity

difference between the two mirrors (for the required high throughput of the bandpass filter), to variations of the environmental conditions (for the necessary precision of the bandpass spectral position control), and to the deviation of the incoming light angle of incidence from normal incidence (for the possibility of imaging applications).

For experimental studies, we measured the FPF transmissivity function using a narrowband emission of He-Ne laser and found a significant broadening of the bandpass with the increase of the filter aperture. By observing a non-uniform cross-sectional distribution of the light intensity in the transmitted non-collimated beam with different maximum-intensity spots at different values of the mirror spacing it can be shown that this effect is due to the mirror non-flatness. We also investigated the dependence of the filter transmissivity on the angle of incidence and found a low sensitivity of this function regarding the aperture width. In addition, we demonstrated an application of the filter width and found the transmissivity function to be the spectral characterization of a broadband diode-laser emission.

Acknowledgments

The authors would like to thank NASA Langley Research Center for their support and funding of this project.

1. H. Buisson, Ch. Fabry, H. Bourget // *Astrophys. J.* **40**, p. 241 (1914).
2. P. Jacquinot // *J. Opt. Soc. Amer.* **44**, p. 76 (1954).
3. V.B. Markov, V. Shishkov, Bragg diffraction with multiple internal reflection // *SPIE Proc.* **1238**, p. 30-40 (1990).
4. V.B. Markov, V. Shishkov, Bragg diffraction with multiple internal Reflection // *Ibid.* **1238**, p. 30-40 (1989).
5. W.B. Cook, H. Snell, P. Hays, Multiplex Fabry – Perot interferometer // *Appl. Opt.* **34**, p. 5263-5277 (1995).
6. H.F. Dobeles, and J.H. Massig, Application of a Fabry – Perot spectrometer to the measurements of spectral line shifts much smaller than line width // *Ibid.* **15**, 69-72 (1976).
7. A.M. Larar, W.B. Cook, and R.S. Lancaster, Laboratory prototype double-etalon Fabry – Perot interferometer for remotely sensing atmospheric ozone // *SPIE Proc.* **3437**, p. 158-166 (1998).
8. W.L. Wolfe, Introduction to imaging spectrometers // *Ibid.* **TT25** (1997).
9. M. Born and E. Wolf, *Principles of optics*, Pergamon, Oxford (1980).
10. R.P. Stanley, C. Weisbuch, *et al.*, Impurity modes in one-dimensional periodic systems: The transition from photonic band gaps to microcavities // *Phys. Rev.* **A48**, p. 2246 (1993).
11. Figotin and V. Gortensveig, Localized electromagnetic waves in a periodic layered dielectric medium with a defect // *Ibid.* **B58**, 180-188 (1998).
12. J.D. Joannopoulos, R.D. Meade, and J.N. Winn, *Photonic crystals*, Princeton University Press, Princeton (1995).
13. D.I. Babic and S.W. Corzine, Analytic expressions for the reflection delay, penetration depth, and absorptance of quarter-wave dielectric mirrors // *IEEE J. Quantum Electron.* **28**, 514–524 (1992).
14. L.R. Brovelli and U. Keller, Simple analytical expressions for the reflectivity and penetration depth of a Bragg mirror between arbitrary media // *Opt. Commun.* **116**, p. 343–350 (1995).
15. E. Garmire, Theory of quarter-wave-stack dielectric mirrors used in a thin Fabry–Perot filter // *Appl. Opt.* **42**, p. 5442-5449 (2003).
16. S. Weidong, L. Xiangdong, H. Biqin, *et al.*, Analysis on the tunable properties of MOEMS filter based on Fabry – Perot cavity // *Opt. Commun.* **239**, p. 153-160 (2004).
17. V. Goren, A. Khizhnyak, and V.B. Markov, *Coupled-wave analysis of the Fabry – Perot interferometer with multi-layer dielectric mirrors accounting losses*, to be published.
18. P. Yeh, *Optical waves in layered media*, Wiley, New York (1988).
19. H. Kogelnik, Coupled wave theory for thick hologram gratings // *BSTJ* **48**, N 9, p. 2909-2947 (1969).
20. J.C. Owens, Optical refractive index of air: dependence on pressure, temperature and composition // *Appl. Opt.* **6**, N 1, p. 51-59 (1967).